THE ROLE OF TIP LEAKAGE FLOW IN SPIKE-TYPE ROTATING STALL INCEPTION

M. Hewkin-Smith*, G. Pullan, S.D. Grimshaw
Whittle Laboratory
University of Cambridge
1 JJ Thomson Avenue
Cambridge, CB3 0DY, UK
Email: mih26@cam.ac.uk

E.M. Greitzer, Z.S. Spakovszky
Gas Turbine Laboratory
Massachusetts Institute of Technology
77 Massachusetts Avenue, 41-205L
Cambridge, MA 02139, USA

ABSTRACT

This paper describes the role of tip leakage flow in creating the leading edge separation necessary for onset of spike-type compressor rotating stall. A series of unsteady multi-passage simulations, supported by experimental data, are used to define and illustrate the two competing mechanisms that cause the high incidence responsible for this separation: blockage from a casing-suction-surface corner separation and forward spillage of the tip leakage jet. The axial momentum flux in the tip leakage flow determines which mechanism dominates. At zero tip clearance, corner separation blockage dominates. As clearance is increased, the leakage flow reduces blockage, moving the stall flow coefficient to lower flow, i.e. giving a larger unstalled flow range. Increased clearance, however, means increased leakage jet momentum and contribution to leakage jet spillage. There is thus a clearance above which jet spillage dominates in creating incidence, so the stall flow coefficient increases and flow range decreases with clearance. As a consequence there is a *clearance for maximum flow range*; for the two rotors in this study, the value was approximately 0.5% chord. The chord-wise distribution of the leakage axial momentum is also important in determining stall onset. Shifting the distribution towards the trailing edge increases flow range for a leakage jet dominated geometry and reduces flow range for a corner separation dominated geometry. Guidelines are developed for flow range enhancement through control of tip leakage flow axial momentum magnitude and distribution. An example is given of how this might be achieved.

INTRODUCTION

There are two scenarios through which the flow in a compressor can make the transition from a nominally axisymmetric flow to the asymmetric regime known as rotating stall. The first involves the growth, over tens of revolutions, of a small amplitude propagating disturbance, with wave length on the order of the circumference, into rotating stall. The initial stage of this evolution is well described by linear stability analysis [1]. The second involves a disturbance with length scale on the order of several blade pitches and a time between initial detection (by casing static pressure measurements, for example) and fully developed rotating stall of less than ten rotor revolutions. The sharp up and down pressure signatures of the disturbance in this type of stall onset have led to them being referred to as spikes [2, 3]. Computational and experimental studies [4–7] have determined that the structure of the spike is a vortex tube, with leading edge separation the source of the vorticity.

In this paper, we use a campaign of computations to explain the causes of the high incidence that create leading edge separation and hence spike-type rotating stall onset. We show there are two mechanisms responsible for this incidence, with competing effects that depend on the tip leakage flow. Figure 1 gives sketches of these two effects.

At zero tip clearance, blockage from a corner separation causes increased incidence in the tip region, as in Fig. 1(a). As the clearance
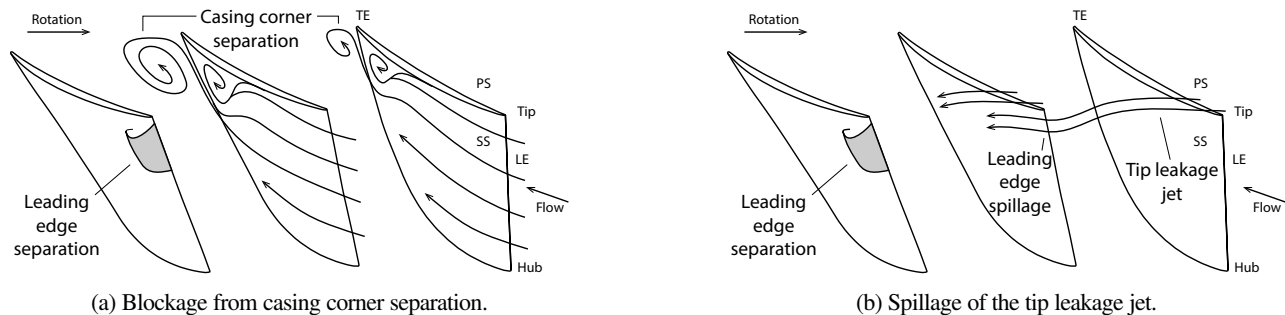

(a) Blockage from casing corner separation.

(b) Spillage of the tip leakage jet.

FIGURE 1: Causes of high incidence that result in leading edge separation.

is opened, the tip leakage flow suppresses the corner separation and the incidence reduces, increasing the flow range of unstalled operation (for brevity, we use the term 'flow range'). Opening the clearance, however, increases the tip leakage flow momentum until the tip leakage jet spills forward of the leading edge of the adjacent blade, causing an incidence increase, as in Fig. 1(b), and decreasing the flow range.

There is thus a non-zero clearance that gives minimum flow coefficient at stall, at which the cause of incidence changes from corner separation blockage to spillage of the leakage jet.

The results to be described encourage an approach to flow range improvement focused on tailoring tip leakage flow axial momentum. The findings also suggest that rather than continually striving to reduce rotor tip clearance, one should seek an optimum tip clearance that provides maximum flow range.

The paper is structured as follows. A summary of the reported link between tip leakage flow and stall onset is provided first. We then present a conceptual description of the mechanisms connecting tip leakage flow and spike-type stall inception, and the approach used to develop this description. Our method of tip leakage flow characterisation is then described. The two causes of high incidence are explained next, and the impacts of tip clearance, and then tip leakage flow distribution, on flow range are illustrated. Finally, the implications of our findings on the design process are considered.

BACKGROUND

Tip leakage flow plays a major role in setting axial compressor stall onset, and efficiency potential, and its importance has spurred a large amount of research. We describe here, at a high level, features relevant for this paper.

Tip leakage flow is driven through the tip clearance by the pressure difference between the pressure and suction sides of the blade. The resulting tip leakage jet, bounded on one side by a shear layer and on the other by the casing, emerges on the suction side at essentially the stagnation pressure at which it entered the clearance. The magnitude of the jet velocity is thus the same as that in the freestream near the suction side [8]. However, because the velocity component along the blade does not change as the flow passes from pressure side to suction side, there is a component of jet velocity normal to the blade and a difference in angle between jet and freestream. As the flow coefficient is reduced, the normal component of velocity increases relative to the component along the blade, so the leakage jet turns towards the upstream direction [9]. The tip leakage jet axial momentum flux captures this behaviour and is thus one feature on which we focus.

Another feature is that the free shear layer in the leakage jet rolls up into a tip leakage vortex, with a core of low (relative frame) stagnation pressure. The core expands as it experiences the blade pressure rise, creating blockage, reducing the pressure rise, and, if the blockage is high enough, causing the pressure rise characteristic to peak and turn over [10]. A peak of the total-to-static pressure rise is associated with the onset of the long-wavelength type of rotating stall inception, so there is direct linkage between tip leakage blockage and this type of stall onset.

Spike-type stall onset occurs on the negatively sloped region of the compressor pressure rise characteristic and is thus not directly driven by tip leakage flow. Pullan et al. [4] have demonstrated that spike type stall inception is associated with local leading edge separation and can occur in a geometry with no tip clearance.

The effect of tip leakage flow on efficiency can also be framed in the context of the above description. Loss is incurred from (i) dissipation of the kinetic energy associated with the component of leakage flow velocity normal to the blade and (ii) the mixing of the velocity defect in the direction along the blade [9].

The above description suggests that increased tip clearance, and hence increased blockage and loss, are detrimental to both efficiency and flow range, and this is borne out over a range of tip clearances of interest in practical devices. It is found, however, that the flow structure in the tip region undergoes a qualitative change as the clearance approaches zero, with blockage and losses becoming associated with separation in the casing-suction-surface corner [11]. For small clearances (various numbers have been reported, but generally less than 1% chord), there can thus be an increase in flow range and peak efficiency for an increase in clearance (see [12–15] and [16–18] respectively, for example).

An explanation for the benefits in efficiency and flow range is that a small amount of tip leakage flow can reduce corner separation through re-energization of the suction-surface boundary layer, as demonstrated by Dong et al. [11] and described by Denton [9]. It seems plausible that both the 'optimums' in flow range and efficiency are associated with the competing effects of separation in the casing-suction corner and tip leakage flow, but it is only the flow range optimum we examine here. We emphasize that we do not claim that the balances between mechanisms are the same for efficiency and stall; these balances may be set by different criteria and occur at different clearances.

Finally, despite the known connections between tip leakage flow and stall, the mechanisms by which the tip leakage flow influences spike-type stall inception have not been established. The cause of the leading edge separation will be shown below to be set by the competing mechanisms of corner separation and of tip leakage flow momentum.

CONCEPTUAL VIEW OF THE ROLE OF TIP LEAKAGE FLOW IN SPIKE-TYPE STALL INCEPTION

To assist discussion of the results, we present a conceptual description of the mechanisms connecting tip leakage flow and spike-type stall inception. The leading edge separation that creates the spike is caused by tip incidence, which is increased by two mechanisms: forward spillage of the tip leakage jet and blockage from casing-suction-surface corner separation. We denote geometries where spillage of the jet is the cause of incidence as 'jet dominated' and geometries where blockage from casing corner separation is the cause of incidence as 'corner separation dominated'.

The relative importance of tip leakage jet spillage and casing corner separation blockage is dependent on tip clearance, as illustrated

in Fig. 2. On the left, with no tip clearance, blockage from the casing corner separation (shown in blue) causes leading edge separation on the adjacent blade. As the clearance increases (moving from left to right in the figure), the leakage flow reduces the corner separation and the momentum of the jet (shown in red) increases. As the tip clearance is increased from zero, suppression of the casing corner separation initially reduces the stall flow coefficient, ϕ_{stall}. The dominant cause of high incidence changes from corner separation blockage to tip leakage jet spillage at the *optimum* tip clearance, where minimum ϕ_{stall} (maximum flow range) occurs. Above this optimum, increase in tip clearance increases both the momentum of the tip leakage jet and ϕ_{stall}.
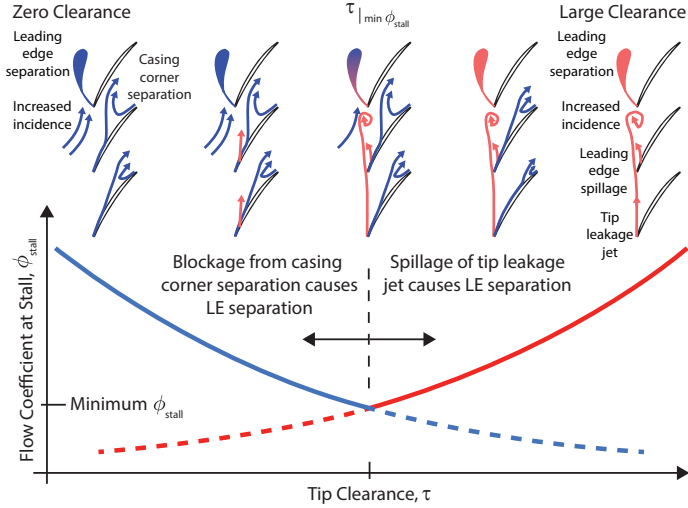

FIGURE 2: Schematics of flow fields that trigger leading edge separation as the tip clearance is increased and stall flow coefficient versus tip clearance. The casing corner separation is suppressed by tip leakage flow as the tip clearance opens, whilst the tip leakage jet strengthens and becomes the incidence mechanism.

APPROACH

The mechanisms that lead to high incidence, presented above, are assessed using a series of numerical experiments with the NASA E^3 Rotor B. In support of the findings, computations are then presented from a second rotor for which a set of experimental data at a range of clearances is available. The approach is described at a high level in this section and full details are given in the Appendix.

The computations are performed using a structured multi-block unsteady Reynolds-averaged Navier-Stokes (RANS) solver with the Spalart-Allmaras turbulence model. Previous studies have shown that unsteady RANS methods are able to qualitatively (spike flow structure and number of stall cells) and quantitatively (pressure-rise characteristics, operating point at stall, and spike propagation speed) capture experimental data, provided that best practice is used for mesh density, domain size and boundary condition treatment [4, 5, 7]. Details of the configuration used in this paper are provided in the Appendix, but here we note the following. The computations have a circumferential extent of six rotor passages; this was found to be sufficient to allow formation of a discrete spike, whilst keeping calculation time and cost to a minimum. The first cells next to all surfaces were within the

laminar sublayer and this led to a mesh count of 1.85 million cells per passage for the E^3 domain. One blade is restaggered by +0.2°, causing an incidence increase equivalent to approximately 1% reduction in flow coefficient, to provide the circumferential non-uniformity necessary for a spike to form. The compressor operating point is controlled using static pressure downstream of an exit nozzle. To change operating point, this exit pressure is ramped - rather than changed in steps - to prevent transients that could lead to premature stall.

Two subsonic rotor geometries are simulated in this paper, with aspect ratios and pitch-chord ratios representative of the mid-to-rear stages of axial compressors in an aeroengine (for the first) and in an industrial gas turbine (for the second).

The first geometry is the E^3 Rotor B, developed by GE and NASA [19]. The E^3 Rotor B has been used for several previous studies of stall inception [4, 6, 20], is known to enter rotating stall through spike-type stall inception and does not exhibit hub or blade surface separations prior to stall [6]. The second geometry, provided by Mitsubishi Heavy Industries, is a low-speed analogue of a gas turbine compressor rotor.

Experimental tests were performed on a single-stage compressor to provide verification of the numerical simulations. Pressure rise characteristics were measured using the gas turbine representative rotor geometry at a series of tip clearances from 0.3% to 3.4% chord. At each clearance, the stall flow coefficient is obtained by averaging ten stall events, with a typical standard deviation of 0.22% of ϕ_{design}. Further details of the test facility and measurement system are given in the Appendix.

TIP LEAKAGE FLOW CHARACTERISATION

We characterise the tip leakage flow using the axial momentum distribution in the tip clearance. The tip leakage flow axial momentum per unit axial chord, Fig. 3, is defined as,

$$\mu = \int_{r_{tip}}^{r_{casing}} \frac{\rho V_n V_x / \cos \alpha}{\dot{m}_{in} V_{x\,in} / c_x} \, dr \,, \qquad (1)$$

where V_n is the tip leakage velocity normal to the suction-surface, α is the local camber angle (such that $dx = dL \cos \alpha$, where dL is chord-wise surface distance), $\dot{m}_{in}$ is the passage inlet mass flow, and the integral is across the tip clearance.

The total tip leakage flow axial momentum, C_μ, is defined as,

$$C_\mu = \int_{x/c_x=0}^{x/c_x=1} \mu \, d\left(\frac{x}{c_x}\right) \,. \qquad (2)$$

We also characterise the distribution of axial momentum in terms of the centroid of the axial momentum distribution, x_μ,

$$x_\mu = \frac{\int_{x/c_x=0}^{x/c_x=1} \mu \frac{x}{c_x} \, d\left(\frac{x}{c_x}\right)}{\int_{x/c_x=0}^{x/c_x=1} \mu \, d\left(\frac{x}{c_x}\right)} \,. \qquad (3)$$

To assess the properties of the tip leakage flow at the same conditions, μ is evaluated at the design operating point for each geometry ($\phi_{design} = 0.407$ for the E^3 Rotor B).
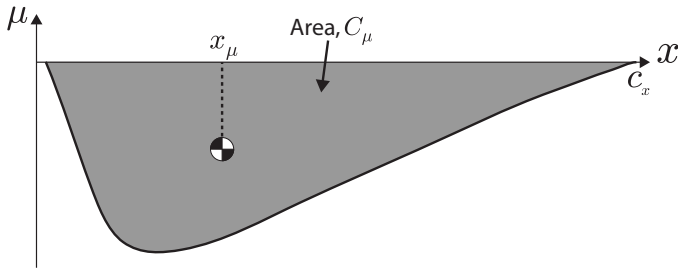

FIGURE 3: Characterisation of the tip leakage flow axial momentum distribution. Integration of the curve provides the total tip leakage flow axial momentum, C_μ, and the centroid, x_μ, is given by Equation 3.

CAUSES OF HIGH INCIDENCE LEADING TO SPIKE-TYPE STALL

We now demonstrate the two mechanisms which can create high incidence using the E^3 Rotor B geometry with: (i) the datum 1.8% chord tip clearance, which is jet dominated, and (ii) without a tip clearance, which is corner separation dominated. The flow fields prior to stall are first described, and then the stall inception process for each geometry, as depicted by the tip flow radial vorticity and simulated casing pressure transducers, is presented.

Near-stall flow field

Figure 4 shows the two distinct flow fields that occur at flow coefficients within 1% of the respective stall flow coefficients. The vortices in the flow are visualised using iso-surfaces of the λ_2 criterion [21].

For the jet dominated geometry (1.8% chord tip clearance), Fig. 4(a), the tip leakage jet fluctuates between attachment to the adjacent pressure surface and the casing in the mid-passage. The jet remains downstream of the leading edge at all times at this flow coefficient. As it oscillates, the jet creates vortical structures that convect downstream and mix out, without impinging on the adjacent leading edge.

For the corner separation dominated geometry (zero tip clearance), there is a three-dimensional separation of the casing and suction-surface boundary layers towards the trailing edge of the blade, Fig. 4(b).

A decrease in flow coefficient of order 1% in *either* of these two flow fields begins the stall inception process, by causing spillage of the tip leakage jet in Fig. 4(a) or growth of the corner separation in Fig. 4(b).

Leading edge separation and spike formation

To demonstrate the processes that lead to stall, Fig. 5 shows contours of radial vorticity at 95% span for one rotor revolution as stall inception occurs, with and without tip clearance. Times are
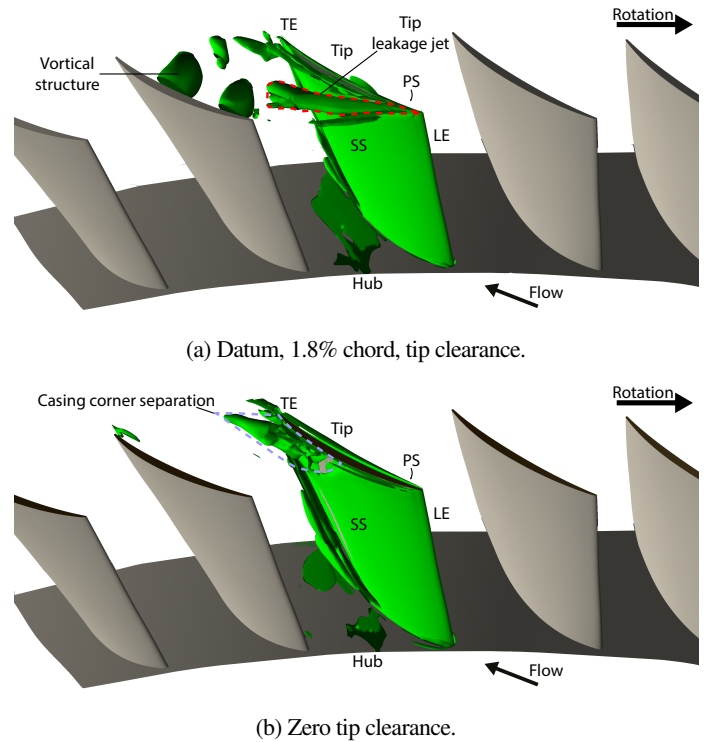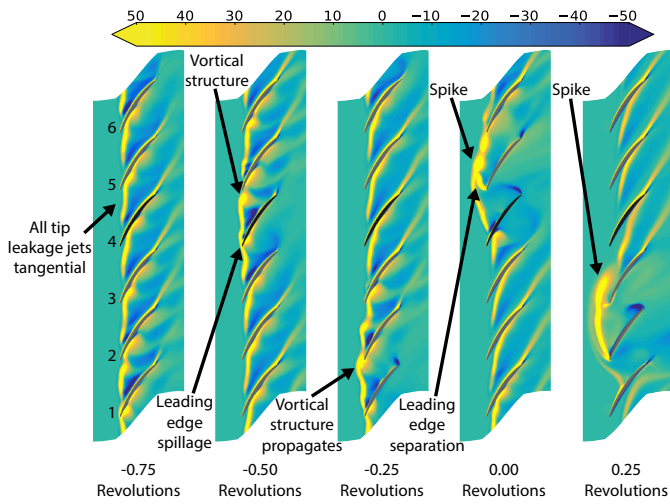

(a) Datum, 1.8% chord, tip clearance.

(b) Zero tip clearance.

FIGURE 4: λ_2 criterion isosurfaces with a contour level of -2×10^6 for an instantaneous point in time immediately prior to stall.
(a) With the datum tip clearance, the tip leakage jet is tangential, and there is no corner separation at the trailing edge of the suction-surface.
(b) With zero tip clearance, casing corner separation occurs.

stated relative to the time of the first leading edge separation. The mechanisms are consistent with those in Fig. 1.

For the jet dominated case, Fig. 5(a), a perturbation in the local flow coefficient causes the tip leakage jet to move upstream, spilling forward of the leading edge at t = -0.5 revs. This spillage interacts with the adjacent tip leakage flow and a circumferentially propagating vortical structure forms. At t = -0.25 revs, the vortical structure has grown in size and at t = 0.00 revs it triggers a leading edge separation on blade five; the shear layer from this separation rolls into a radial vortex, which is the spike. The spike continues to grow and affects nearly two passages by t = +0.25 revs.

For the corner separation dominated case, Fig. 5(b) shows that the largest blockage is from the corner separation on blade four (the restaggered blade). The separation on blade four grows between t = -0.75 revs and t = -0.25 revs, and the blockage in passage four-five increases the incidence onto blade five, so the separation there also grows. The increased blockage within passages four-five and five-six diverts more flow into the other passages, suppressing their separations. At t = 0.00 revs, the separation on blade five blocks the entire pitch of the passage at the radial location shown. The blockage causes a large enough incidence increase onto blade six to trigger leading edge separation, creating a radial vortex, the spike, which propagates to blade three and grows in size, by t = +0.25 revs. From t = 0.00 revs onwards, irrespective of the cause of high incidence, the qualitative structure and the development of the spike is the same.

(a) Datum, 1.8% chord, tip clearance. $\phi_{stall} = 0.370$
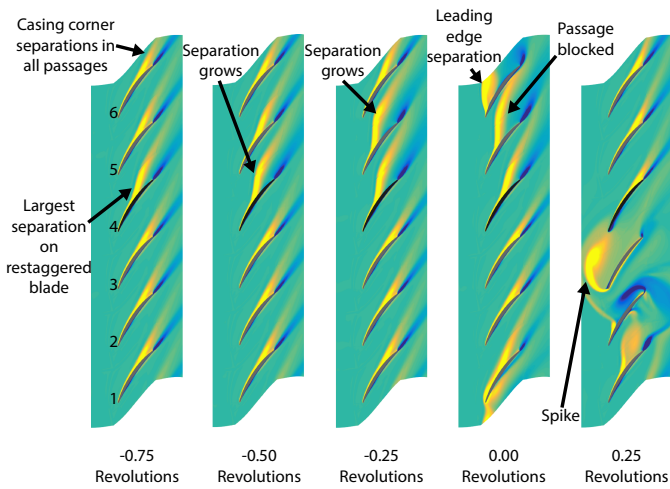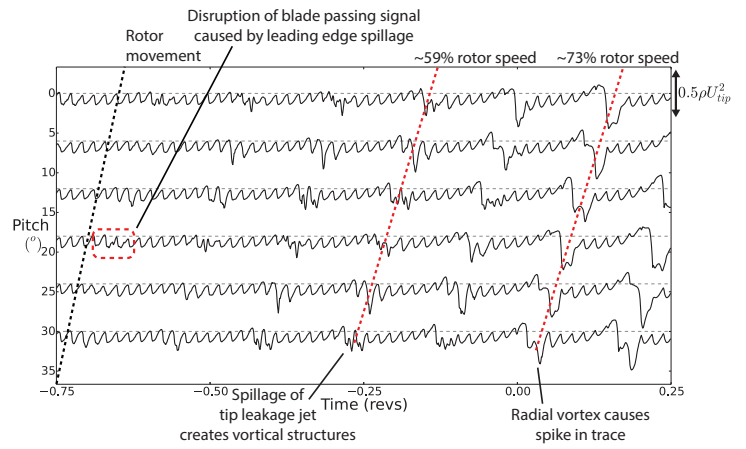

(b) Zero tip clearance. $\phi_{stall} = 0.347$

FIGURE 5: Contours of radial vorticity at 95% span for E^3 Rotor B, (a) with tip clearance and (b) without tip clearance, as stall occurs. (a) Spillage of the tip leakage jet in front of the leading edge creates propagating vortical structures. These structures grow until they cause leading edge separation. (b) Casing corner separations grow on blades four and five, causing leading edge separation of blade six.

Pressure traces from simulated casing transducers

Spikes were first observed experimentally using a circumferential array of fast-response casing pressure transducers [2]. In correspondence with this, plots of casing total-to-static pressure coefficient at 5% chord upstream of the leading edge for six simulated transducers, spaced one pitch apart, are given in Fig. 6.

Disruption in the blade passing signal, caused by the leading edge spillage, is detected in the pressure traces for the datum clearance case, Fig. 6(a), at t = -0.65 revs. The spike appears (between -0.10 and 0.00 revs) as the leading edge separation occurs.

In the corner separation dominated case, Fig. 6(b), there is no disruption to the blade passing signals prior to t = -0.25 revs, because there is no tip leakage jet. Modulations of the signal, between

(a) Datum, 1.8% chord, tip clearance.
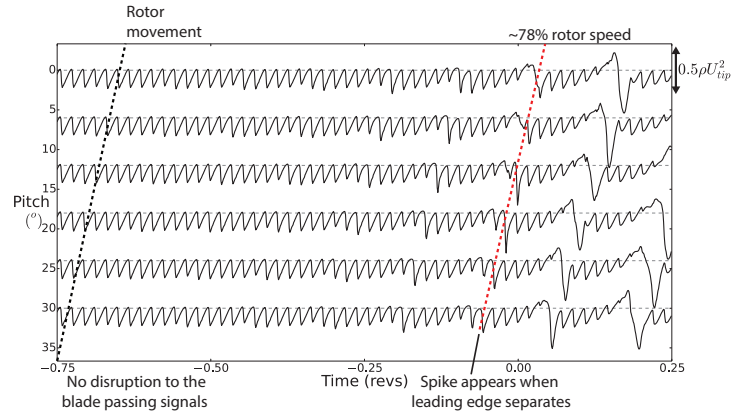
(b) Zero tip clearance.

FIGURE 6: Simulated traces of casing total-to-static pressure coefficient 5% chord upstream of the rotor leading edge. (a) With the datum tip clearance, the traces are recognisable as spike-stall development. (b) Without tip clearance the traces show no warning prior to the leading edge separation and spike-stall development.

t = -0.25 revs and t = -0.05 revs, are apparent as the casing corner separations grow.

After leading edge separation has occurred (t = -0.05 revs to 0.00 revs) the casing pressure traces with and without tip clearance are similar: a leading edge separation causes a spike which propagates at 73% and 78% rotor speed respectively.

Summary concerning mechanisms for high incidence

The computations show the two causes of the high incidence that triggers spike-type stall inception. The first is spillage of the tip leakage jet forward of the leading edge, illustrated by the datum (1.8% chord) tip clearance E^3 Rotor B case. The second is blockage from a casing-suction-surface corner separation, shown by the zero tip clearance case. Once the leading edge separation has occurred, the qualitative development of the spike is the same.

THE IMPACT OF TIP CLEARANCE ON STALL FLOW COEFFICIENT

We now extend the set of E^3 Rotor B computations to 12 different clearances, to provide specifics concerning the effects of clearance on flow range. The stall points are presented first, followed by the balance of the two incidence mechanisms as the clearance is changed. The section concludes with a set of computations and experiments for the gas turbine representative rotor, where qualitatively similar results are obtained.

Optimum tip clearance for maximum flow range

Figure 7 shows a chart of total-to-static pressure rise coefficient versus flow coefficient for the computations of the E^3 Rotor B at tip clearances from zero to 3.0% chord. The locus of stall points is indicated by the heavy line. Four pressure rise characteristics are also shown (for zero, 0.5%, 1.8% and 3.0% chord tip clearance). The optimum clearance, at which the flow range is maximised, is 0.5% chord. We define the flow range, $\Delta\phi$, as the difference between design point ($\phi_{design} = 0.407$) and stall point flow coefficient, $\Delta\phi = \phi_{design} - \phi_{stall}$.

As the tip clearance is increased from zero ($\Delta\phi = 0.060$), the flow range increases, to a maximum at 0.5% chord ($\Delta\phi = 0.106$). Further increases in clearance reduce the flow range until, at clearances greater than 1.6% chord, the flow range becomes a weak function of clearance ($\Delta\phi = 0.045 \pm 0.008$). Such independence of flow range at large clearances has been reported previously, for example in Hunter and Cumpsty [22]. At clearances above the optimum (0.5% chord), the pressure rise at stall is consistent with the monotonic variation with tip clearance presented by Koch [23]. However, we show here that, for the E^3 Rotor B, as the clearance is reduced below 0.5% chord, the stall pressure rise falls as the clearance tends to zero.

Figure 8 identifies the dominant cause of high incidence at each clearance. The figure provides a quantitative depiction of the conceptual description in Fig. 2. Flow range is maximised at 0.5% chord tip clearance for the E^3 Rotor B. At smaller clearances the cause of incidence is blockage from casing corner separation. At larger clearances the cause of incidence is spillage of tip leakage jet. For all clearances, leading edge separation is the cause of spike inception.

Changes to the flow field as tip clearance is varied

The change in flow field as the clearance is increased can be seen in the radial vorticity contours in Fig. 9. The contours are at 95% span for 0.3% and 0.5% chord clearances (corner separation dominated), and 0.7% and 0.9% chord clearances (jet dominated).

The 0.3% and 0.5% chord tip clearance cases at $\phi = 0.308$ both display casing corner separations, Fig. 9(a) and (b). The corner separation is smaller with 0.5% chord clearance, because the increased tip leakage flow energises the suction-surface boundary layer more than at 0.3% chord clearance. The 0.3% chord clearance case stalls at a higher flow coefficient than the 0.5% chord clearance ($\Delta\phi_{0.3\%} = 0.099$, $\Delta\phi_{0.5\%} = 0.106$).

The 0.7% and 0.9% chord tip clearance cases at $\phi = 0.329$ are shown in Fig. 9(c) and (d). The 0.9% chord clearance geometry has a leakage jet oriented more tangentially than the 0.7% chord clearance
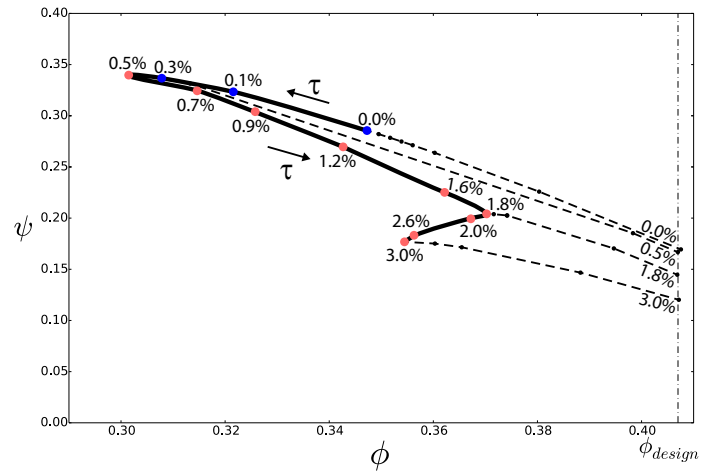
FIGURE 7: Total-to-static pressure rise coefficient characteristics for a selection of tip clearance from 0.0% to 3.0% chord. The heavy line marks the locus of stall points at the different tip clearances.
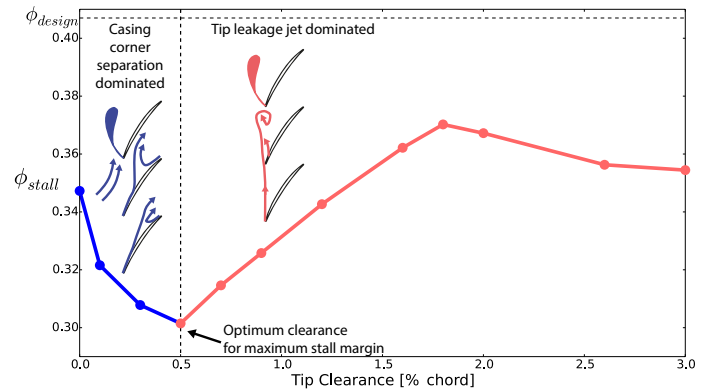
FIGURE 8: Tip clearance versus stall flow coefficient for the E^3 Rotor B. Three regions of stall point behaviour exist: Increase in flow range due to suppression of casing corner separation, reduction in flow range due to strengthening of tip leakage jet and weak dependence of flow range on tip clearance.

geometry. The 0.7% chord clearance geometry reaches lower flow coefficients than the 0.9% chord clearance before the tip leakage jet spills ahead of the leading edge ($\Delta\phi_{0.7\%} = 0.092$, $\Delta\phi_{0.9\%} = 0.081$).

The change in tip leakage flow axial momentum with tip clearance provides insight into the independence of flow range from tip clearance at clearances above 1.6% chord. The magnitude of design point tip leakage flow axial momentum, $|C_\mu|$, normalised by the tip clearance as a proportion of rotor tip chord, τ, increases as the tip clearance is opened from 0.0-1.6% chord, Fig. 10. At clearances greater than 1.6% chord, $|C_\mu|/\tau$ is approximately constant at 0.64 ± 0.01, i.e. $|C_\mu|$ increases in proportion to the clearance. The impact of the tip leakage flow on the rotor tip flow field is only a weak function of clearance at clearances above 1.6% chord, so the flow range is approximately constant.
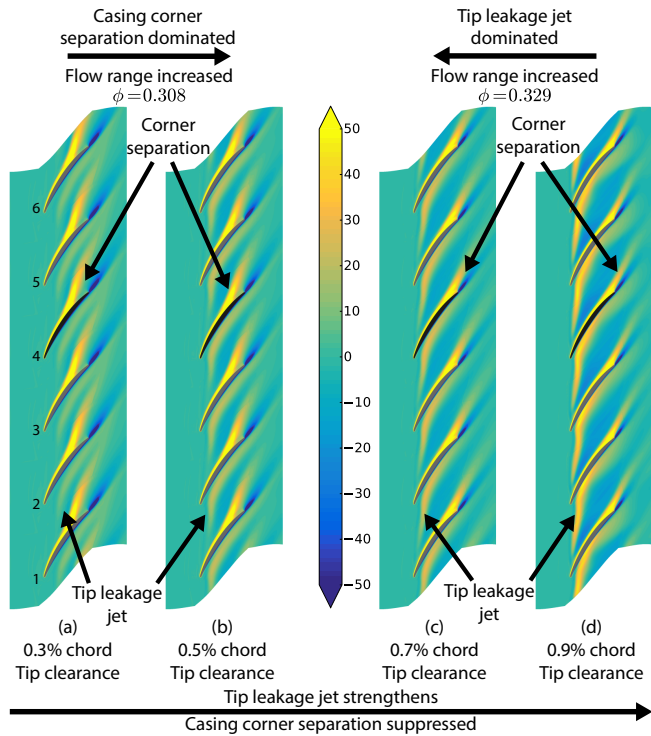
FIGURE 9: Instantaneous radial vorticity contours at 95% span for, (a) and (b), two corner separation dominated clearances at $\phi = 0.308$ and, (c) and (d), two jet dominated clearances at $\phi = 0.329$. Opening the clearance suppresses the casing corner separation, but increases the momentum of the tip leakage jet.
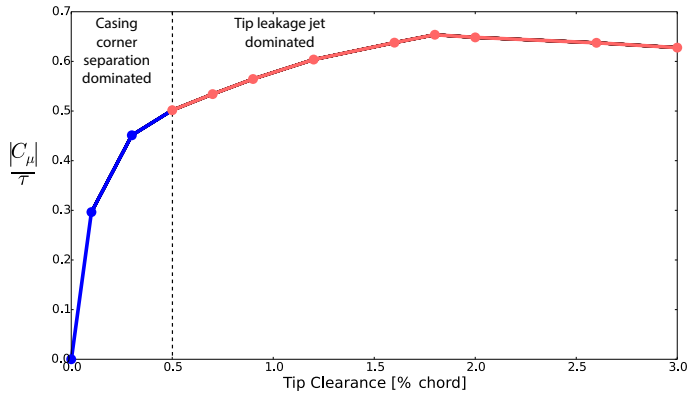

FIGURE 10: Tip leakage flow axial momentum flux, normalised by tip clearance, as a function of tip clearance. The momentum flux increases in magnitude as tip clearance is increased from 0.0% to 1.6% chord, but is constant at larger clearances. This correlates with the change in flow range, when spillage of the leakage jet is the incidence mechanism.

Experimental comparison for a second rotor geometry

Figure 11 shows experimental and computational stall flow coefficient as a function of tip clearance for the gas turbine representative rotor geometry, which has a design flow coefficient of 0.385. The two parametric trends - the existence of an optimum clearance and reduced sensitivity to clearance at large clearances - are consistent with the E^3 results. The experimental results match the computational
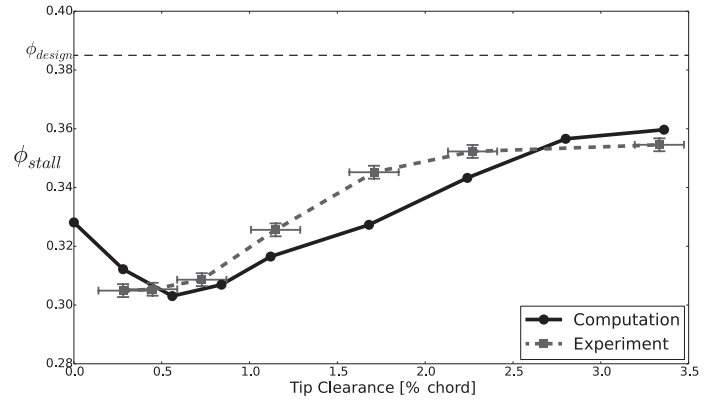

FIGURE 11: Stall flow coefficient as a function of tip clearance for experiments and computations of the gas turbine representative rotor. In the experimental data, horizontal error bars indicate circumferential variation in tip clearance, vertical error bars show three standard deviations of the stall points at each clearance. The results match with an average error of 1.9% ϕ_{design}.

results with an average error of 1.9% ϕ_{design}, with errors in part due to the eccentricity of $\pm 0.15\%$ chord that is found at all clearances. The underlying mechanisms in the computed flow field (not shown) are also consistent with the conceptual description in Fig. 2. At zero clearance for the gas turbine rotor, $\Delta\phi = 0.057$ and blockage from casing corner separation causes leading edge separation. The maximum flow range occurs at a tip clearance of 0.6% chord ($\Delta\phi = 0.082$). Above this optimum clearance, jet spillage is the dominant cause of incidence, and the flow range is reduced with increased clearance.

Summary concerning the effect of tip clearance on stall flow coefficient

Unsteady computations for an aeroengine compressor rotor, and computations and experiments for a compressor rotor representative of an industrial gas turbine, have shown the effects of tip clearance on the flow coefficient of spike-type rotating stall onset. There is a minimum stall flow coefficient at a non-zero tip clearance. Interrogation of the computations shows that the mechanism responsible for the leading edge incidence, and thus the spike-type rotating stall inception, changes from blockage due to casing corner separation at small clearances to spillage of the tip leakage jet at large clearances.

THE IMPACT OF TIP LEAKAGE FLOW DISTRIBUTION ON FLOW RANGE

We have described the effect of tip clearance on flow range based on changes in the *magnitude*, $|C_\mu|$, of tip leakage flow axial momentum. In this section, we determine the influence of the chord-wise *distribution* of tip leakage flow axial momentum, μ. We characterise the distribution using its centroid, x_μ. To change the distribution of the leakage flow, the clearance is progressively blocked off from the leading edge, creating a 'part-chord' clearance. We first report the effects on the datum 1.8% chord clearance and then, using part-chord clearances from a range of tip clearances, determine the effect of changing the μ distribution at a fixed value of $|C_\mu|$.
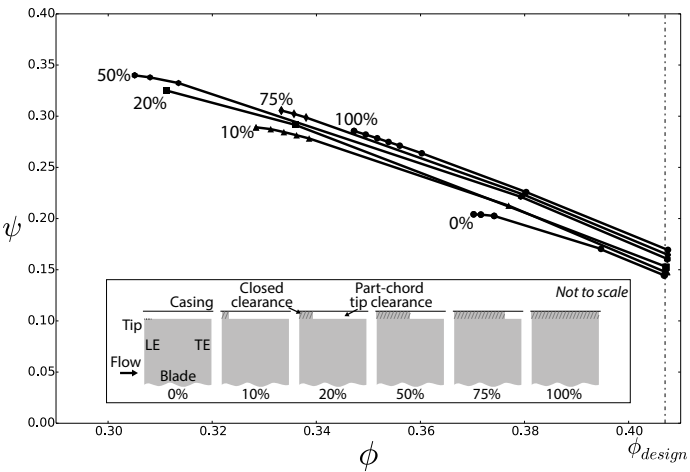
Part-chord tip clearances at 1.8% chord clearance

As the leading section of the clearance is blocked more and more, sketched in Fig. 12(b), the peak momentum region of the jet is shifted towards the trailing edge and aligned further towards the downstream direction. The trough of the μ distribution is shifted towards the trailing edge as more of the clearance is closed, Fig. 12(a). $|C_\mu|$ is reduced by 23%, 42% and 87% by the closure of the leading 10%, 20% and 50% chord of the tip clearance respectively and is near zero when the leading 75% chord of the tip clearance is closed.

Figure 12(b) shows the total-to-static pressure rise characteristics for the 1.8% chord part-chord tip clearances. With the full 1.8% chord tip clearance, tip leakage jet spillage dominates. As the leading section of the tip clearance is closed, the tip leakage flow is forced further downstream of the leading edge and the flow range improves. For example, closure of the leading 10% of the tip clearance improves the flow range by 114% (from $\Delta\phi = 0.037$ to 0.079). Closure to 50%
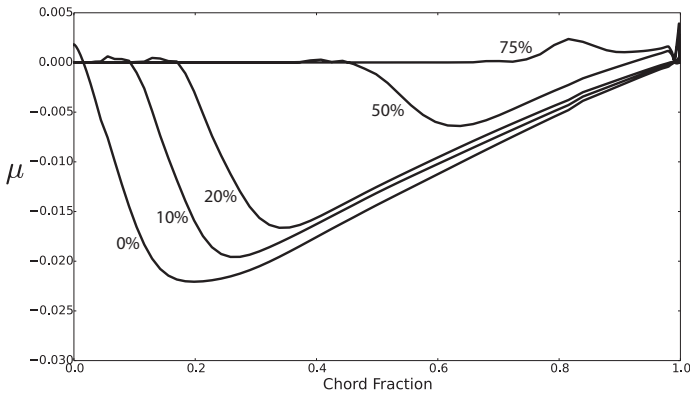
(a) Tip leakage flow axial momentum distributions for 1.8% chord part-chord tip clearances.

(b) Total-to-static pressure rise characteristics for 1.8% chord part-chord tip clearances. *Inset:* Schematic of the tip clearance, as the leading section is progressively closed.

FIGURE 12: Closing the leading section of the 1.8% chord tip clearance shifts the μ distribution towards the trailing edge and reduces $|C_\mu|$. Up to 50% closure this improves the flow range. Beyond 50% closure, the dominant incidence mechanism is blockage from casing corner separation, so further closure reduces flow range.

chord improves the flow range by an additional 46% (to $\Delta\phi = 0.102$); at this condition, the cause of incidence is casing corner separation blockage. If the extent of the closed clearance is increased beyond 50% chord, the reduced leakage flow becomes less effective at suppressing the corner separation, and the flow range reduces (at 75% closure, $\Delta\phi = 0.074$). As the clearance is closed further, the characteristics tend toward the zero clearance result.

### The effect of tip leakage flow distribution at fixed magnitude

Closing the leading section of the tip clearance changes the μ distribution, but it also changes $|C_\mu|$. Using a database of computations of part-chord tip clearances over a range of clearances (37 configurations were used in support of this study), we can assess the effect of changing the shape of the μ distribution at approximately fixed $|C_\mu|$. Anticipating that the consequences will be dependent on whether the full-chord tip clearance is a leakage jet spillage or a corner separation blockage dominated geometry, two sets of cases are considered.

The first set is the datum 1.8% chord tip clearance and a 3.0% chord tip clearance with the leading 20% chord of the tip clearance closed (denoted 20-100%). Spillage of the tip leakage jet is the cause of incidence in both cases. The μ distributions are given in Fig. 13(a). The 3.0% part-chord clearance has shifted x_μ by 15% chord towards the trailing edge of the blade, $|C_\mu|$ is within 4.3% $|C_\mu|_{datum}$. The shift in x_μ causes the 3.0% part-chord tip clearance flow range to increase by 126% compared to the datum clearance case ($\Delta\phi$ increases from 0.037 to 0.083).

The second set of cases are 0.7% chord tip clearance, 1.2% chord tip clearance with the leading 30% chord of the tip clearance closed (denoted 30-100%), and 3.0% chord tip clearance with the leading 45% chord of the tip clearance closed (denoted 45-100%). Fig. 13(b) shows the μ distributions for these cases. The range of $|C_\mu|$ is within 3.4% $|C_\mu|_{datum}$, but the distributions are different. The full-chord 0.7% chord tip clearance is jet dominated. x_μ moves from 32% chord at 0.7% chord tip clearance, to 49% chord with the 1.2% part-chord clearance, to 70% chord with the 3.0% part-chord clearance. Changing from the 0.7% chord clearance to the 1.2% part-chord clearance results in 14.0% flow range improvement ($\Delta\phi$ increases from 0.092 to 0.105). At a distribution between that of the 1.2% part-chord clearance and the 3.0% part-chord clearance, the dominant incidence mechanism changes from leakage jet spillage to casing corner separation blockage. Shifting the distribution further, as in the 3.0% part-chord clearance, thus results in less effective suppression of the corner separation, with flow range reduced by 3% compared to the 1.2% part-chord clearance ($\Delta\phi$ decreasing from 0.105 to 0.102).

Summary of the impact of tip leakage flow distribution on flow range

Shifting the distribution of a *jet* dominated geometry towards the *trailing edge* increases the flow range, because the tip leakage jet moves further downstream of the leading edge. Shifting the distribution of a *corner separation* dominated geometry towards the *leading edge* increases the flow range, due to suppression of casing corner separation.
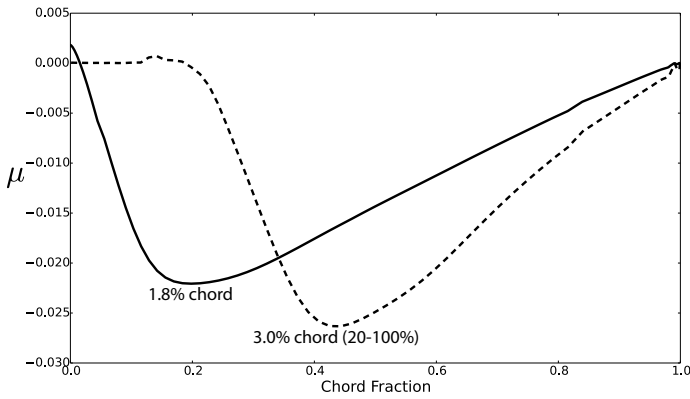
(a) Tip leakage flow axial momentum distributions for 1.8% chord and 3.0% chord 20-100% part-chord tip clearances. The aft-shift in μ distribution improves the flow range by 126%.
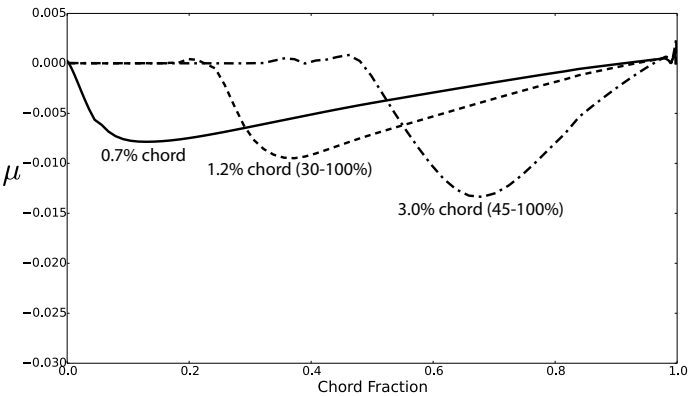
(b) Tip leakage flow axial momentum distributions for 0.7% chord, 1.2% chord 30-100% part-chord and 3.0% chord 45-100% part-chord tip clearances.

FIGURE 13: Tip leakage flow axial momentum distributions for two sets of geometries where the $|C_\mu|$ are equivalent in each set, but the distributions different.

IMPLICATIONS FOR THE DESIGN PROCESS

The findings we have described suggest it would be useful, in designing for flow range improvement, to consider the tip leakage flow axial momentum distribution. Also, the goal should be to determine the clearance for maximum flow range, rather than to reduce the tip clearance as much as possible.

Steady computations, at the design operating point, can characterise the tip leakage flows of candidate geometries. The most promising geometries can then be selected for examination by unsteady stall calculations, based on their tip leakage flow characterisation, allowing more effective use of resources during the design process.

The approach outlined above was used to identify a 3D rotor design to improve the flow range of the E^3 Rotor B, at the datum 1.8% chord tip clearance. A parametric study of sweep, dihedral and leading edge recamber, using steady calculations at the design point, was conducted to establish suitable levels of each technique to both reduce $|C_\mu|$ and aft-shift x_μ. The example geometry discussed here employed 15% chord forward sweep, 10% chord negative dihedral (using the same definitions as [24]), a +5° recamber of the leading edge and

+1.25° restagger to recover lost pressure rise. The stated values of sweep, dihedral and recamber are the values for the tip section, and the geometry blends back to the datum by 75% span. The calculated design point total-to-total isentropic efficiency for the 3D geometry was 0.12 percentage points higher than that of the datum geometry.

Figure 14 shows (a) the blade shapes, (b) the change to the tip leakage flow axial momentum distribution and (c) the pressure rise characteristic as predicted by unsteady calculations, for the datum and example 3D geometries. The 3D design achieved a 22% reduction in $|C_\mu|$ and 13% chord aft-shift of x_μ and the changes to the tip leakage flow axial momentum distribution resulted in a 90% flow range improvement.

SUMMARY AND CONCLUSIONS

Two causes of the high incidence that triggers spike-type rotating stall have been identified. One is blockage from a casing-suction-surface corner separation; the other is spillage of the tip leakage jet in front of the leading edge plane. The axial momentum in the tip leakage flow determines which of these two mechanisms occur.

At zero tip clearance, corner separation blockage is the dominant mechanism. As the clearance is increased, the axial momentum of the leakage flow reduces this blockage and the flow range increases. Increasing the clearance, however, also increases the momentum in the leakage jet and at the clearance for maximum flow range both causes of incidence occur at the same flow coefficient. For the E^3 Rotor B, this optimum clearance is 0.5% chord. At clearances above this, the leakage jet becomes the dominant cause of incidence and further increase in clearance reduces the flow range, until a clearance is reached (1.6% chord for the E^3) above which there is minimal change in flow range.

The computations show that the chord-wise distribution of the tip leakage flow axial momentum, as well as the total magnitude, is important in characterising the leakage flow. For a given tip leakage flow axial momentum, shifting the distribution towards the trailing edge improves the flow range of a leakage jet dominated geometry and reduces the flow range of a corner separation dominated geometry.

The computations imply that control of both the magnitude and distribution of the tip leakage flow axial momentum may have potential for use in flow range improvement. Candidate designs can be assessed by comparing the tip leakage flow axial momentum distributions at the design point, requiring only steady calculations. An example given for the E^3 Rotor B (which has a design point flow coefficient of 0.407), with a 1.8% chord tip clearance, used 3D design techniques to produce a 22% reduction in tip leakage flow axial momentum magnitude and a shift of the centroid of the tip leakage flow axial momentum distribution by 13% chord towards the trailing edge. Unsteady stall point calculations gave a computed reduction in stall flow coefficient from 0.370 to 0.337, a flow range improvement of 90%.

(a) Datum and 3D designed E^3 Rotor B.

(b) Tip leakage flow axial momentum distributions for datum and 3D designed E^3 Rotor B geometries.

(c) Total-to-static pressure rise coefficient characteristics for the datum and 3D designed E^3 Rotor B geometries.

FIGURE 14: Implementation of an example 3D design of the E^3 Rotor B reduces $|C_\mu|$ and shifts the distribution towards the trailing edge, improving the flow range by 90% ($\Delta\phi$ increases from 0.037 to 0.070).

APPENDIX
Computational approach

The description given here is for E^3 Rotor B calculations, values for the gas turbine representative rotor (GTRR), if different, are given in parentheses. The structured multi-block Reynolds Averaged Navier-Stokes solver *Turbostream* [25], was used for all the computations in this project. The code uses finite-volume time-marching, second order in space, with three levels of multi-grid and a single step explicit time integration scheme. All simulations use the Spalart-Allmaras turbulence model with adaptive wall functions and fully turbulent boundary layers. Unsteady simulations are second order accurate in time using Jameson's dual time-stepping technique.

All calculations are rotor-only and the meshes were created using Numeca's *Autogrid*™. An O-4H block topology was employed around the blade and the tip mesh uses an O-H topology. The blade O-mesh uses 217 (GTRR: 313) nodes around the blade surface and there are 89 nodes in the radial direction throughout the domain. All blocks are rotating, removing the need for mixing/sliding planes; the casing is kept stationary. The grid density is set such that the adaptive wall functions operate in the laminar sub-layer region (typical $y_+ < 5$).
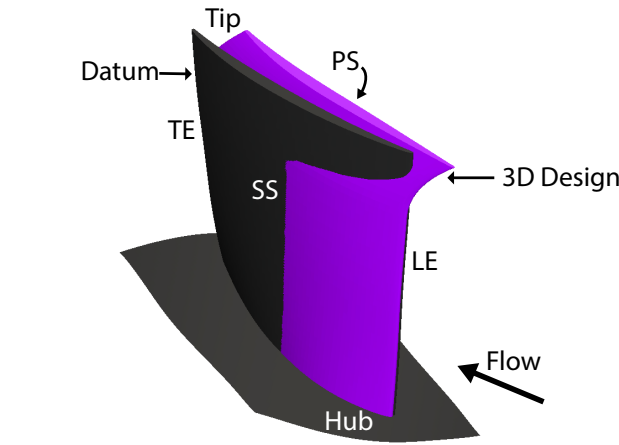
20 span-wise cells are used in the tip clearance for datum tip clearance geometry configurations; the same stall point was found when using more span-wise cells in the tip clearance. Additional cells were added to resolve the tip leakage flow at larger clearances.

The computational domain for the datum geometry, with 1.85 million (GTRR: 2.27 million) cells per blade passage, uses a converging nozzle at the exit to allow operating point adjustment on flat parts of the pressure rise characteristic [26]. The inlet plane is positioned 3.6 (GTRR: 7.1) blade tip pitches upstream of the leading edge, with the outlet 3.6 (GTRR: 7.1) blade pitches downstream of the trailing edge, plus 4.7 (GTRR: 15.2) further blade pitches for the converging nozzle and exit block.
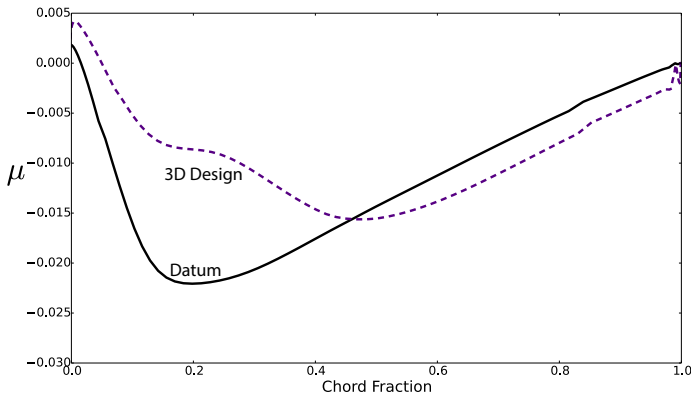
Unless otherwise stated, all inlet properties are taken from an inlet plane 0.8 (GTRR: 1.21) axial chords upstream of the rotor leading edge and all exit properties are taken from an outlet plane 5.5 (GTRR: 0.7) axial chords downstream of the trailing edge to allow for mixing to occur.

At the inlet, a stagnation pressure profile with displacement thickness, $\delta^* = 3.6\%$ span, and momentum thickness, $\theta = 3.0\%$ span, and a relative yaw angle profile were implemented. (GTRR: The stagnation pressure and yaw angle profiles were matched with an experimental measurement taken 1.25 axial chords upstream of the rotor leading edge at the design point with 1.1% chord clearance.)

An investigation of the effect of number of passages was conducted on the datum geometry with the objective of capturing the emergence of the spike whilst minimising computational time. It was found that a discrete spike was unable to form when using less than six passages, as it impinges on itself via the periodic sector boundary and creates a non-physical result. The six passage calculation allows sufficient circumferential space for a spike to form, and therefore six blade passages, a 40° sector (GTRR: 37° sector), have been used for all calculations in this paper. Whilst six passages are sufficient
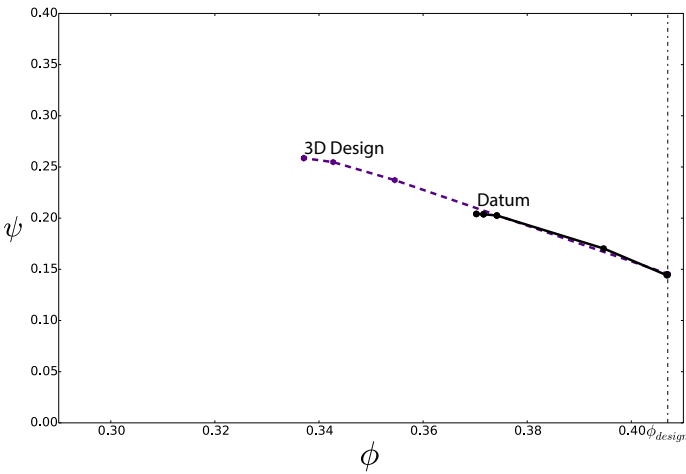
for this stall inception study, more passages would be required to investigate the development of the final rotating stall flow field.

The fidelity of stall flow coefficient determination is chosen to be 1% ϕ_{design}. Operating point is changed using a ramp in back pressure to prevent premature stall due to transients. Each operating point is then held constant for three revolutions to check for stall inception. The lowest stable-operating flow coefficient is run for at least eight rotor revolutions to ensure stall inception does not begin. The stall flow coefficient is taken as the lowest stable-operating flow coefficient.

Circumferential non-uniformity in flow solution between blade passages is needed to capture spike-type stall inception. A 0.2° restagger is used to increase incidence of one of the six blades (blade #4), for all unsteady calculations. This restagger angle is approximately the incidence change produced by a change in flow coefficient of 1% ϕ_{design}.

Hub-to-tip radius ratio	0.75
Number of rotor blades	58
Number of stator blades	60
Stator hub tip clearance	1.0% stator chord
ϕ_{design}	0.43
ψ_{design}	0.50
Tip Mach number	0.23
Rotor Reynolds number	1.6×10^5
Casing diameter	0.51 m

TABLE 1: Single-stage compressor rig geometry details.

Experimental approach

A low speed, single-stage compressor rig has been used to verify the numerical simulations at varying tip clearances using the gas turbine representative rotor geometry. Inlet swirl is provided by a row of inlet guide vanes and the stator blades are cantilevered. Other details of the compressor are in Table 1.

Rotor blade tip clearance is varied from 0.3% chord (0.10 mm) to 3.4% chord, by progressively cutting back the tips of the blades. The rotor tip clearance is measured when the machine is running to within ±0.003% rotor tip chord, using a fast-response laser displacement sensor mounted in the compressor casing. The variation in tip radius when the rig is running at design speed is typically ±0.06% rotor tip chord. Casing rings are concentric to within ±0.09% rotor tip chord. Thus the total circumferential variation of the rotor tip clearance is ±0.14% rotor tip chord; this is due to manufacturing and assembly tolerances and rig vibration.

Traverses are performed 1.25 axial chords upstream of the rotor row, using a five-hole probe with head diameter of 1.6% span, to provide a measured inlet profile for computations. The rig includes four pneumatically averaged inlet Pitot tubes upstream of the inlet guide vane row and static pressure tappings upstream and downstream of the stage. Air temperature is measured with thermocouples, atmospheric pressure with a digital barometer and rig speed using a tachometer. Together with an inlet calibration from the area traverse these measurements were used to determine flow coefficient and total-to-static pressure rise coefficient. Rig operating point is varied using a downstream throttle. The stall flow coefficient is obtained by averaging ten stall events, with a typical standard deviation of 0.22% of ϕ_{design}.

NOMENCLATURE

A_{in}	Inlet area
c	True chord (tip)
C_μ	Total tip leakage flow axial momentum
$C_p = \frac{p - p_{01}}{\frac{1}{2}\rho_{in}U_{tip}^2}$	Total-to-static pressure coefficient
c_x	Axial chord (tip)
GTRR	Gas Turbine Representative Rotor
LE	Leading edge
$\dot{m}_{in}$	Inlet mass flow rate, per passage
p	Static pressure
p_{01}	Mass-averaged inlet stagnation pressure
p_{02}	Mass-averaged exit stagnation pressure
p_2	Area-averaged exit static pressure
PS	Pressure surface
r	Radius
r_{casing}	Casing radius
r_{tip}	Tip radius
revs	Rotor revolutions
SS	Suction-surface
t	Time, rotor revolutions
T_{01}	Mass-averaged inlet stagnation temperature
T_{02}	Mass-averaged exit stagnation temperature
$T_{02s} = T_{01}\left(\frac{p_{02}}{p_{01}}\right)^{\frac{\gamma-1}{\gamma}}$	Isentropic exit stagnation temperature
TE	Trailing edge
U_{tip}	Blade speed at tip
V_n	Velocity normal to suction-surface
V_x	Axial velocity
$V_{x\,in} = \frac{\dot{m}_{in}}{\rho_{in}A_{in}}$	Area-averaged inlet axial velocity
x	Axial distance, measured from the rotor LE
x_μ	Centroid of μ distribution
α	Local camber angle
γ	Ratio of specific heat capacities
$\Delta\phi = \phi_{stall} - \phi_{design}$	Flow range
$\eta = \frac{T_{02s} - T_{01}}{T_{02} - T_{01}}$	Total-to-total isentropic efficiency
μ	Tip leakage flow axial momentum, per unit axial chord
$\phi = \frac{V_{x\,in}}{U_{tip}}$	Flow coefficient
$\psi = \frac{p_2 - p_{01}}{\frac{1}{2}\rho_{in}U_{tip}^2}$	Total-to-static pressure rise coefficient
ρ	Density
ρ_{in}	Area-averaged inlet density
τ	Tip clearance (as proportion of tip chord)
stall	Stall point
design	Design point

REFERENCES

[1] Garnier, V. H., Epstein, A. H., and Greitzer, E. M., 1991. "Rotating waves as a stall inception indication in axial compressors". *ASME J. Turbomach,* **113**(2), April, pp. 290–301.

[2] Day, I. J., 1993. "Stall inception in axial flow compressors". *ASME J. Turbomach,* **115**, Jan, pp. 1–9.

[3] Emmons, H. W., Pearson, C. E., and Grant, H. P., 1955. "Compressor surge and stall propagation". *Transactions of the ASME*, pp. 455–469.

[4] Pullan, G., Young, A. M., Day, I. J., Greitzer, E. M., and Spakovszky, Z. S., 2015. "Origins and structure of spike-type rotating stall". *ASME J. Turbomach,* **137**(5), May, p. 051007.

[5] Yamada, K., Kikuta, H., Iwakiri, K., Furukawa, M., and Gunjishima, S., 2013. "An explanation for flow features of spike-type stall inception in an axial compressor rotor". *ASME J. Turbomach,* **135**(2), Nov, p. 021023.

[6] Vo, H. D., Tan, C. S., and Greitzer, E. M., 2008. "Criteria for spike initiated rotating stall". *ASME J. Turbomach,* **130**, Jan, pp. 1–9.

[7] Dodds, J., and Vahdati, M., 2015. "Rotating stall observations in a high speed compressor part ii: Numerical study". *ASME J. Turbomach,* **137**(5), May, p. 051003.

[8] Storer, J. A., and Cumpsty, N. A., 1990. "Tip leakage flow in axial compressors". *ASME J. Turbomach,* **113**(2), Apr, pp. 252–259.

[9] Denton, J. D., 1993. "Loss mechanisms in turbomachines". *ASME J. Turbomach,* **115**, Oct, pp. 621–656. 1993 IGTI Scholar Lecture.

[10] Khalid, S. A., Khalsa, A. S., Waitz, I. A., Tan, C. S., Greitzer, E. M., Cumpsty, N. A., Adamczyk, J. J., and Marble, F. E., 1999. "Endwall blockage in axial compressors". *ASME J. Turbomach,* **121**, Jul, pp. 499–509.

[11] Dong, Y., Gallimore, S. J., and Hodson, H. P., 1987. "Three-dimensional flows and loss reduction in axial compressors". *ASME J. Turbomach,* **109**(3), Jul, pp. 354–361.

[12] Wennerstrom, A. J., 1984. "Experimental study of a high-throughflow transonic axial compressor stage". *ASME J. Eng. Gas Turbines Power,* **106**, Jul, pp. 552–559.

[13] McDougall, N. M., Cumpsty, N. A., and Hynes, T. P., 1990. "Stall inception in axial compressors". *ASME J. Turbomach,* **112**, Jan, pp. 116–123.

[14] Wisler, D. C., Beacher, B. F., and Shin, H.-W., 2002. "Effects of loading and clearance variation on tip vortex and endwall blockage". In Proc. 9th International Symposium in Transport Phenomena and the Dynamics of Rotating Machinery, Honolulu, Hawaii, February 10-14.

[15] Zhang, Z., Yu, X., and Liu, B., 2012. "Characteristics of the tip leakage vortex in a low-speed axial compressor with different rotor tip gaps". In Proc. ASME Turbo Expo, Jun 11-15, Copenhagen, Denmark, Volume 8: Turbomachinery, Parts A, B, and C, pp. 311–322.

[16] Cumpsty, N. A., 1989. *Compressor Aerodynamics*. Krieger Publishing Company. p. 343-352.

[17] Lakshminarayana, B., and Horlock, J. H., 1965. "Leakage and secondary flows in compressor cascades." Aeronautical Research Council Reports and Memoranda 3483, Ministry of Technology, March.

[18] Gbadebo, S. A., 2003. "Three-dimensional separations in axial compressors". PhD thesis, University of Cambridge.

[19] Wisler, D. C., 1977. "Core compressor exit stage study: Volume i–blade design". *NASA CR135391*.

[20] Nolan, S. P. R., 2005. "Effect of radial transport on compressor tip clearance flow structures and enhancement of stable flow range". Master's thesis, Massachusetts Institute of Technology.

[21] Jeong, J., and Hussain, F., 1995. "On the identification of a vortex". *J. Fluid Mech,* **285**, Feb, pp. 69–94.

[22] Hunter, I. H., and Cumpsty, N. A., 1982. "Casing wall boundary-layer development through an isolated compressor rotor". *ASME J. Eng. Power,* **104**, Oct, pp. 805–818.

[23] Koch, C. C., 1981. "Stalling pressure rise capability of axial flow compressor stages". *ASME J. Eng. Power,* **103**, Oct, pp. 645–656.

[24] Gallimore, S. J., Bolger, J. J., Cumpsty, N. A., Taylor, M. J., Wright, P. I., and Place, J. M. M., 2002. "The use of sweep and dihedral in multistage axial flow compressor blading-part ii: Low and high-speed designs and test verification". *ASME J. Turbomach,* **124**(4), Nov, pp. 533–541.

[25] Brandvik, T., and Pullan, G., 2011. "An accelerated 3d navier-stokes solver for flows in turbomachines". *ASME J. Turbomach,* **133**(2), Oct, p. 021025.

[26] Vahdati, M., Sayma, A., Freeman, C., and Imregun, M., 2005. "On the use of atmospheric boundary conditions for axial-flow compressor stall simulations". *ASME J. Turbomach,* **127**, Aug, pp. 349–351.